Long Duration Aeroacoustic Simulations

By

Dilhara Jayasundara

AMSC/CMSC-664 - Final Report

Advisor: Prof. James Baeder

May 2021

Contents

List of Figures

List of Tables

1 Introduction

The future of air travel is increasingly dominated by urban air mobility (UAM), where large numbers of electric vertical take off and landing (eVTOL) aircraft flying within and between large cities is expected to be commonplace. NASA describes its goal of UAM is to have a safe and efficient air transportation system where everything from small package delivery drones to passenger-carrying air taxis operate over populated areas, from small towns to the largest cities [1]. It further describes its vision on UAM as "taking air travel to the streets, or just above them" as portrayed by Figure 1.1. Currently, there are about 150 companies that are in the business of producing eVTOLs that could potentially be able to fly around major cities transporting passengers and goods in the coming decade. Uber, which is among the leading companies, is planning to start commercial operations of its UAM program "Uber Elevate" in Dallas, Los Angeles, and Melbourne as quickly as 2023 [3].

Figure 1.1: An artist's conception of an urban air mobility environment, where air vehicles with a variety of missions and with or without pilots, are able to interact safely and efficiently [1]

The main source of thrust for these eVTOL aircraft is propellers, mainly due the small size and light weight. Most eVTOL designs include multiple propellers located in close proximity to one another in order to provide both vertical and horizontal forces needed to fly the aircraft. Propellers

are viewed as cost-effective sources of propulsion for small commuter aircraft with fuel savings of 10-20% compared to turbofan engines [4]. However, one main drawback of propeller-driven aircraft is the high noise levels [5], produced not only by the propellers themselves but also due to interactions of the propeller slipstream with the wing surface. Earlier, propellers were powered by internal combustion engines, which also generated a significant noise themselves. With improvements in battery technology and energy storage future propeller driven aircraft are designed to be powered by electric motors, which emit a significantly lower noise than engines. Therefore, aircraft noise is dominated by the aerodynamic noise of propellers and airframe. Aircraft noise is considered a critical challenge to the UAM industry as it can cause serious threats to both passenger and pedestrian comfort in urban environments, diminishing public acceptance.

Meanwhile, there is ongoing research on transform conventional fossil fuel based large aircraft to ones that are powered by electric or hybrid electric propulsion systems. The main objectives are to decrease emissions, fuel usage and noise levels. This is an important step towards having a sustainable future of air travel amid the growing number of aircraft flying around the world. NASA is leading the research work by experimenting on the X-57 Maxwell, an all-electric aircraft named after the Scottish physicist James Clerk Maxwell, shown in Figure 1.2. It is aimed at modifying an Italian Tecnam P2006T aircraft by replacing the two piston engines with an electric propulsion system consisting of 14 electric motors. Daher, Airbus and Safran have also teamed up to develop Ecopulse™, a distributed hybrid propulsion aircraft demonstrator to battle noise and emissions in order to meet the future needs of air travel industry and for the development of environmental-friendly, cleaner aviation.

Figure 1.2: NASA X-57 Maxwell aircraft [2]

Both UAM and hybrid-electric propulsion require aircraft noise reduction to be dealt with an entirely different approach and much more seriousness than ever before. With mechanical noise being less important, the prominent source of noise becomes the aerodynamics of the propellers or rotors. Rotor noise can be divided into two components, ie., discrete frequency noise and broadband noise. Discrete frequency noise include thickness, loading, high-speed impulsive and quadrupole noise.

Thickness noise is caused by a displacement in air due to blade motion, whereas loading noise is caused by an accelerating force distribution. These two components add up to the tonal noise, of which the frequency of the fluctuating pressure depends on the rotor frequency. High-speed impulsive and quadrupole noise components are negligible in subsonic speeds, at which, most eVTOLs operate. Broadband noise is mainly caused by the turbulent boundary layer of the blade surface. Even though, this is negligible in high-speed aircraft, it has become an important component in low-speed aircraft such as eVTOLs. The main driving factor of propeller noise is found to be the tip speed, which is highly related to the thickness noise [6]. Therefore, the main approach to aircraft noise reduction is distributing the thrust produced by a single propeller to multiple propellers operating at much lower tip speeds.

Due to the high demand for quieter eVTOLs, reducing aircraft noise has become more painstaking than ever before. Understanding the physics behind noise generation at different aerodynamic surfaces and their combined effect towards the total aircraft noise is very important and has been conventionally done using wind tunnel tests and flight tests. However, with the development of computational fluid dynamics, computational tools can be used to numerically simulate noise generation and propagation from any aerodynamic surface, which is very convenient in investigating multiple cases in a short period of time. An analytical solution exists for tonal noise in the event of simple aircraft motions, and for complex cases, a numerical approach can be used. Broadband noise has to be modelled with empirical formulae.

2 Computational Aeroacoustics

The main governing equation of computational aeroacoustics is the Ffowcs Williams - Hawkings (FW-H) equation [7]. This is mainly an inhomogeneous form of the wave equation obtained by manipulating the Navier-Stokes and mass conservation equations.

2.1 Ffowcs Williams - Hawkings Equation

Consider a volume V as given in Figure 2.1, which is divided into two regions, ie.,1 and 2, by a closed surface S. $\mathbf{n}$ and $\mathbf{l}$ are the unit normal vectors to surface S and the surface that contains volume V, which is Σ. The flow velocity is $\mathbf{u}$ and the velocity of surface S is $\mathbf{v}$.
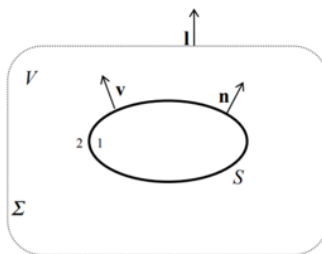

Figure 2.1: Fluid domain

The rate of change of mass within V is given by,

$$\frac{\partial}{\partial t} \int_V \overline{\rho} dV = -\int_\Sigma (\overline{\rho u_i}) l_i d\Sigma + \int_S [\rho(u_i - v_i)]_2 \, n_i dS - \int_S [\rho(u_i - v_i)]_1 \, n_i dS \tag{1}$$

Here, ρ is the local density and the overbar implies that the variable is to be regarded as a generalized function valid throughout V. By divergence theorem,

$$\int_V \left(\frac{\partial \overline{\rho}}{\partial t} + \frac{\partial}{\partial x_i} (\overline{\rho u_i}) \right) dV = \int_S [\rho(u_i - v_i)]_2 \, n_i dS - \int_S [\rho(u_i - v_i)]_1 \, n_i dS \tag{2}$$

If $f = 0$ defines surface S, such that $f < 0$ is in region 1 and $f > 0$ is in region 2, the surface integral on the right hand side can be converted to a volume integral using the Kronecher delta function δ_{ij}.

$$\int_V \left(\frac{\partial \overline{\rho}}{\partial t} + \frac{\partial}{\partial x_i} (\overline{\rho u_i}) \right) dV = \int_V \left([\rho(u_i - v_i)]_2 - [\rho(u_i - v_i)]_1 \right) \delta(f) \frac{\partial f}{\partial x_i} dV \tag{3}$$

By dropping the volume integrals, the generalized mass conservation equation can be obtained.

$$\frac{\partial \overline{\rho}}{\partial t} + \frac{\partial}{\partial x_i} (\overline{\rho u_i}) = [\rho(u_i - v_i)]_1^2 \, \delta(f) \frac{\partial f}{\partial x_i} \tag{4}$$

Similarly, the generalized momentum conservation equation can also be obtained.

$$\frac{\partial}{\partial t} (\overline{\rho u_i}) + \frac{\partial}{\partial x_j} (\overline{\rho u_i u_j} + \overline{p}_{ij}) = [p_{ij} + \rho u_i (u_i - v_i)]_1^2 \, \delta(f) \frac{\partial f}{\partial x_i} \tag{5}$$

Here, p_{ij} is the compressive stress tensor and $[\ ]_1^2$ means the difference of the contents between region 2 and 1. Here, S represents a solid surface in the impermeable formulation and therefore, u_i in region 1 should be zero. Also, the density and pressure in region 1 are equal to freestream values. In region 2, $u_n = v_n$ due to the impermeability condition. Taking the spatial derivative of Eq. 5 and subtracting it by the time derivative of Eq. 4 gives the Ffowcs Williams - Hawkings equation shown in Eq. 6.

$$\left(\frac{\partial^2}{\partial t^2} - c^2 \frac{\partial^2}{\partial x_i^2} \right) \overline{\rho'} = \frac{\partial}{\partial t} \left(\rho_0 v_i \delta(f) \frac{\partial f}{\partial x_i} \right) - \frac{\partial}{\partial x_i} \left(p_{ij} \delta(f) \frac{\partial f}{\partial x_i} \right) + \frac{\partial \overline{T_{ij}}}{\partial x_i \partial x_j} \tag{6}$$

The left hand side of Eq. 6 is the wave equation, where c is the speed of sound given by $c = \sqrt{\frac{p}{\rho}}$, and the right hand side provides the source terms. The first term denotes the thickness source, which is a monopole in nature and generates acoustic pressure due to displacement of air volume by the surface $f = 0$. The second term, which is a dipole, indicates the loading source, which relates to acceleration of the loading distribution on the surface $f = 0$. The last term is a quadrupole source, which relates to the Lighthill stress tensor, T_{ij}, given by,

$$T_{ij} = \rho u_i u_j + p_{ij} - c^2 (\rho - \rho_0) \delta_{ij} \tag{7}$$

It has been shown that this term can be neglected for subsonic flow conditions, where the Mach number is much lower than 1 [8].

2.2 Farassat's Formulation 1 and 1A of the FW-H equation

The FW-H equation is solved using the free-space Green's function of the wave equation. Farassat's formulation 1 of the FW-H equation is given in Eq. 8. The derivation can be found in Farassat, 2007 [9].

$$4\pi p'(\mathbf{x},t) = 4\pi(p_T'(\mathbf{x},t)+p_L'(\mathbf{x},t)) = \frac{\partial}{\partial t}\int_{f=0}\left[\frac{\rho_0 v_n}{r(1-M_r)}+\frac{p\cos\theta}{cr(1-M_r)}\right]_{ret}dS+\int_{f=0}\left[\frac{p\cos\theta}{r^2(1-M_r)}\right]_{ret}dS \tag{8}$$

Here, p_T' and p_L' are the fluctuating components of the thickness and loading acoustic pressure that are generated by the respective sources. r is the distance between the observer location and the source element in consideration. M is the local Mach number of the surface and M_r implies the component in the direction of the observer, ie., the radiation direction. p is the surface pressure and θ is the local angle between surface normal and the radiation direction. $[\ ]_{ret}$ denotes that the contents inside the inside the brackets are to be take at the retarded time, which is the corresponding source time, τ, at which the pressure signal was emitted. Therefore, all the variables need to be taken at the source time, τ, corresponding to the respective observer time, t, when the acoustic pressure is calculated. The relationship between τ and t is given in Eq. 9

$$t = \tau + \frac{r}{c} \tag{9}$$

Farassat's formulation 1 formulation includes an observer time derivative which has to be calculated numerically. This increases the execution time on the computer and reduces the accuracy of the results [9]. Therefore, Farassat came up with an alternative formulation by converting the observer time derivative into a source time derivative and was named as Farassat's forumulation 1A of the FW-H equation. The thickness and loading acoustic pressure equations are given in Eq. 10 and 11, respectively.

$$4\pi p_T'(\vec{x},t) = \int_{f=0}\left[\frac{\rho_0(\dot{v}_n+v_{\dot{n}})}{r(1-M_r)^2}\right]_{ret}dS + \int_{f=0}\left[\frac{\rho_0 v_n(r\dot{M}_r+c(M_r-M^2))}{r^2(1-M_r)^3}\right]_{ret}dS \tag{10}$$

$$4\pi p_L'(\vec{x},t) = \frac{1}{c}\int_{f=0}\left[\frac{\dot{l}_r}{r(1-M_r)^2}\right]_{ret}dS + \int_{f=0}\left[\frac{l_r-l_M}{r^2(1-M_r)^2}\right]_{ret}dS + \frac{1}{c}\int_{f=0}\left[\frac{l_r(r\dot{M}_r+c(M_r-M^2))}{r^2(1-M_r)^3}\right]_{ret}dS \tag{11}$$

Here, $\vec{l}$ denotes the local force per unit area acting on the fluid given by $l_i = p_{ij}n_j$.

2.3 The Acoustic Code of the University of Maryland (ACUM)

ACUM is based on Farassat's formulation 1A of the Ffowcs Williams - Hawkings equation, and is used to compute the tonal noise emissions of an aerodynamic surface by numerical integration.
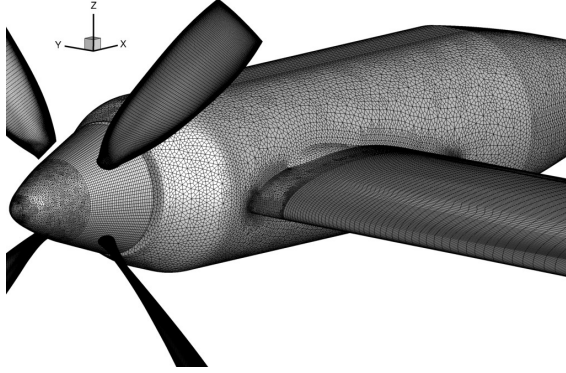
(a) Sample geometry - wingtip-mounted propeller
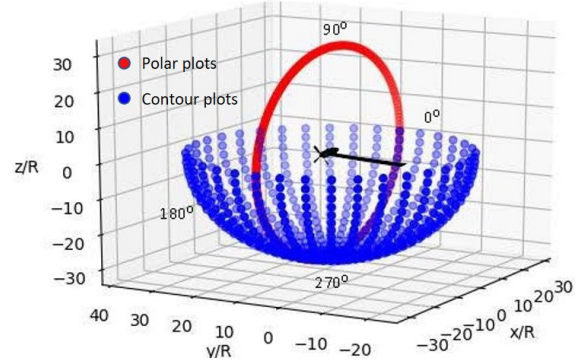
(b) Observer locations

Figure 2.2: Sample geometry and corresponding observer locations

There are two versions of the code, with slight differences from each other, with regard to functionality. ACUM-1, which is written in Fortran, can only be used to simulate blade geometries with explicitly defined airfoil shapes. The compact chord approximation, where the blade loads are concentrated at the $1/4^{th}$ chord location and the thickness source and sink are placed at the $1/8^{th}$ and $5/8^{th}$ chord locations, is used in this code for acoustic computations. Blade loads are calculated by the Blade Element Momentum Theory [10]. Therefore, this assumes that the blade loading changes only in the span-wise direction, which is not too wrong from an acoustic perspective. However, this approximation can only be used for rotor blades, and hence, this version cannot be used to compute the acoustic signature of other aerodynamic surfaces.

ACUM-2, which is written in CUDA for the purpose of reducing the computation time by parallelizing on GPUs, can be used to compute the acoustics of any geometric surface. The surface loads are calculated using CFD simulations of the geometry. The acoustic pressure computation is carried out by numerically integrating the acoustic pressure generated by each surface element. This integration is carried out in a discrete form, with both the geometric surfaces and the time dimension being discretized. The acoustic pressure is computed at multiple observer locations surrounding the geometry. A sample geometry and the corresponding observer location are given in Figure 2.2. Currently, it is able to parallelize observer locations and surface elements but has not been able to obtain time-step parallelization due to the double time loop method used in the forward in time approach.

ACUM is only capable of simulating periodic events, where the input variables have a period equal to the time taken for one propeller revolution. Therefore, this period is divided into 360 time steps and the input data is considered at each time step. Acoustic pressure is also calculated at each time step for one propeller revolution and this data is used to calculate the overall sound pressure level (OASPL) at each observer location in dB using Eq. 12.

$$OASPL = 20 log_{10} \left[\frac{p - p_{mean}}{p_{ref}} \right] \tag{12}$$

2.4 Forward in Time Approach

In ACUM, the retarded time calculation in the Farassat's 1A formulation is carried out by a forward in time approach. It first calculates the acoustic pressure and the corresponding observer time at each source time step. Then, it runs through a second time loop to map each time step to the corresponding source time using the previously calculated observer times at each time step, and interpolates the solution from the nearest two neighbors. Therefore, for each element, it has to go through two time loops, and therefore, the time dimension cannot be parallelized on GPU.

3 Project Description

A comprehensive approach to aircraft noise reduction should not only look into the noise generation and propagation from aerodynamic surfaces, but also needs to consider the practical aspects of aircraft operations. As eVTOLs are expected to take-off and land at highly congested urban locations, the acoustic signatures of these maneuvers must be taken into consideration when designing a quieter aircraft. Moreover, eVTOLs and most future aircraft will likely to have multiple propellers located in close proximity to each other. Some of the designs have changes in the propeller orientations as the aircraft switches between the helicopter and airplane mode. Most of them change the rotational speed of the propellers in maneuvering the aircraft. These are not necessarily periodic events, which can be represented by input data for one propeller revolution. Analysing the acoustics of these non-periodic events require acoustic simulations to be run for thousands of propeller revolutions, which the current code is not capable of. ACUM-2 takes about 10-15 minutes to calculate the acoustic pressure time history for one revolution, for the wingtip-mounted propeller shown in Figure 2.2(a). At this rate, a thousand revolution computation, which is equivalent to about 10 seconds of flying time, would take up to 10 days. Therefore, a new version of ACUM needs to be developed that can compute the acoustic pressure for a large number of propeller revolutions at a much faster rate. Increase in computational speed can only be achieved by parallelizing the time steps, together with the observer locations and source elements.

3.1 Binning Approach

Binning approach [11] is an alternative to the double-time loop method used in the forward in time approach. In the double-time loop method, the interpolation is done in the second time loop, which is from the observer's perspective. In the binning approach, the solution is binned into the nearest two observer time steps. An equally spaced source timeline results in an unequally spaced observer timeline. Therefore, the total fraction of the hits received by each observer time step will not be equal to one. Hence, the solution at each observer time step has to be divided by its total fraction of hits, which needs to be done in a separate time loop. This second time loop can be avoided by calculating the observer times for the two neighboring time steps at each source time step. Thereby, the correct fraction of the solution can be calculated and binned to the corresponding observer time step, without having to divide by the total fraction. Therefore, each time step can carry out the computation independent from other time steps, and hence, the time dimension can be parallelized.

3.2 Development of ACUM-3

The main objective of the project is to develop a new version of the acoustic code, ACUM-3, that has the capability to compute acoustic pressure time histories at different observer locations for large number of time steps. An important aspect of this version is to have time step parallelization so that the large number of time steps will not significantly affect the computation time. This can be done using the binning approach instead of the current double-time loop approach. A 3D GPU parallelization for time steps, observer locations, and source elements can save a significant amount of computation time, while increasing the efficiency of the code.

The other concern is the massive amount of input data that has to be handled before and within the computation. Currently, input data is loaded using a separate file for each surface that contains geometric and pressure data for each element at each time step. A CFD mesh contains about 20,000 to 50,000 elements based on the geometric and aerodynamic features of the surface. Having 360 time steps per revolution, these input file sizes are of the order of 1 GB, and therefore, that into thousand times will essentially lead to memory issues. This can be avoided by looking into the possibility of doing part of the computation inside the CPU and reducing the number of time steps per revolution without significantly compromising accuracy. A single GPU is unlikely to handle so much of data in its memory or to perform the computation in a reasonable amount of time. Therefore, it is necessary to look into the possibility of distributing the work load across multiple GPUs using MPI (Message Passing Interface). A high performance computing (HPC) cluster can be used for running the code.

3.3 Modifications to CFD solver

The project also requires certain modifications to the in-house CFD solver, HAMSTR [12]. At the moment, it is unable to simulate non-linear geometric movements and rotational speed variations. Therefore, this capability has to be added to the CFD solver in order to simulate the non-periodic aircraft movements. Moreover, CFD requires a finer mesh with reduced element sizes at locations with rapid variations in geometry or which are of aerodynamic importance. This is important to prevent numerical diffusion as well as to capture small scale turbulent structures. However, the acoustic analysis does not necessarily need a finer mesh as the one needed for CFD. A coarser mesh can be used to do the surface integration computation without having to compromise accuracy. Currently, there is a post-processing script that tries to coarsen the CFD mesh and average the input data onto the coarsened mesh. With large number of time steps, this has to be done inside the CFD solver and therefore, it is necessary to use two meshes in the CFD solver, ie., the finer mesh for the computation and the coarser mesh for the averaged data to be saved on. This would also avoid the need for post-processing of the CFD output in order to fit the data into the acoustic solver.

3.4 Validation

Validation of ACUM-3 can be done using the results of ACUM-2, which has been already validated in previous studies [13]. The propeller geometry in Figure 2.2(a), which consists only of the 4 blades can be used in the for this purpose. The model geometry was obtained from the 1st AIAA Workshop for Integrated Propeller Predictions (WIPP) [14]. First, the binning approach has to be tested by implementing it on ACUM-2. Comparison between the results from the current approach and the binning approach is required for this purpose. Then, once the coding of ACUM-3 is over,

the acoustic pressure time history can be computed for only one propeller revolution from the two versions of ACUM and compared with each other. This should ensure that ACUM-3 is free from any potential bugs. Finally, the acoustic pressure time history can be computed on ACUM-3 for multiple revolutions of level flight and compared with the ACUM-2 results for one revolution. As level flight provides periodic acoustic pressure time history ACUM-2 results should be equal to ACUM-3 results at any period. The OASPL of the propeller at the circular observers defined in Figure 2.2(b) is given in Figure 3.1. The observers are located 30 propeller radii away from the propeller center and are fixed respect to the center of the propeller. The acoustic pressure time history at 0° and 90° elevation angles are given in Figure 3.2.
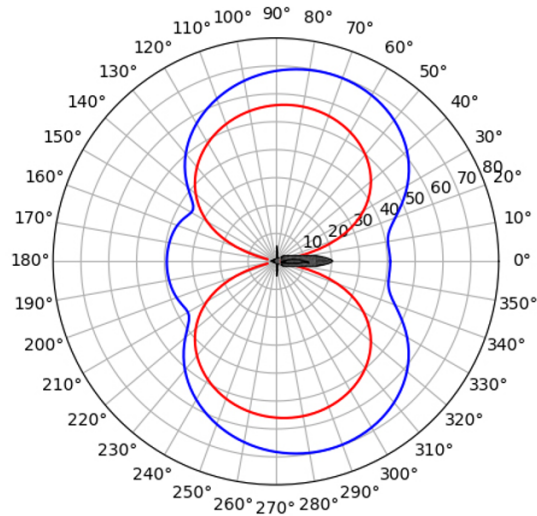

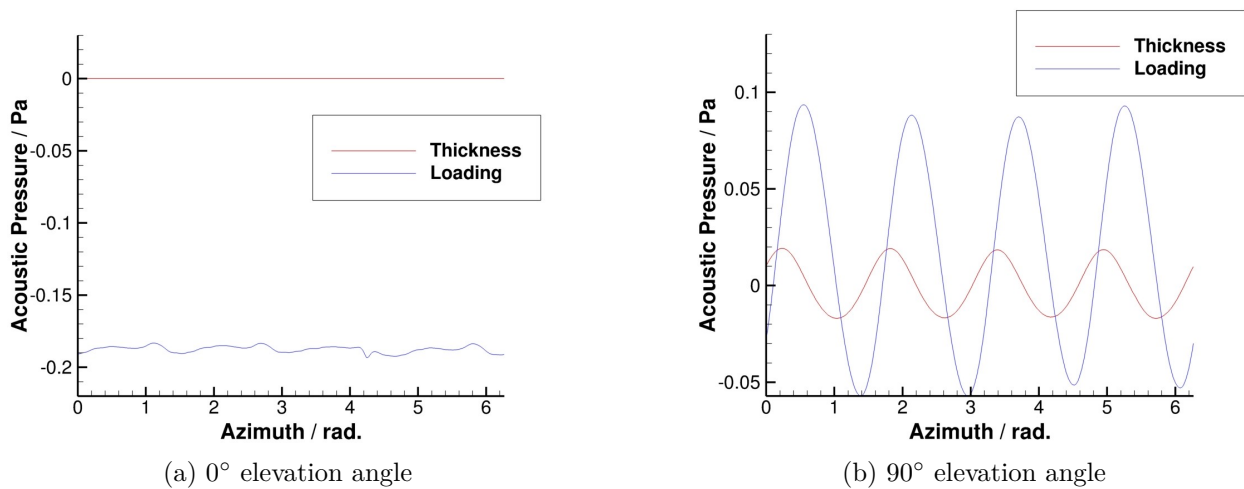Figure 3.1: OASPL in dB for propeller geometry from ACUM-2

(a) 0° elevation angle

(b) 90° elevation angle

Figure 3.2: Acoustic pressure time history for propeller geometry from ACUM-2

3.5 Simulation of Non-Periodic Cases

Once ACUM-3 is validated, it can be used to run non-periodic cases with multiple propeller revolutions. The main focus would be on simulating aircraft maneuvers such as flyovers, take-offs, landings turns etc. Depending on whether the aircraft comes towards the observer or goes away from it, the noise levels felt at the observer location could differ significantly. Identifying the acoustic signature of these maneuvers is extremely important in designing future aircraft and landing platforms. In addition to that, changes in propeller rotational speed can also be simulated with a single propeller and also with multiple propellers located next to each other to study their cumulative effect. Based on the phase difference of these propellers, there can be amplifications and cancellations of the total acoustic pressure generated by the aircraft. Moreover, it is also important to investigate the effects of switching between helicopter and airplane modes, where the propeller axes are tilted by a substantial amount. It is possible that a sudden change in propeller orientation causing a change in acoustic pressure at a certain observer location. Each of these cases can be initially simulated only with the propeller blades, and then other parts of the aircraft such as the wings, nacelles and the fuselage can be added.

However, due to the time limitation of the course, the a transition case of a tiltrotor from hover to cruise is simulated covering most of the non-periodic movements such as accelerated transition, accelerated rotation, and rotation within a rotation.

4 Development of ACUM-3

Implimentation of the project begins with writing ACUM-3 with 3D GPU parallelization and MPI parallelization. Measures were taken to reduce the computation time a well. Upon validation, the flyover case was run for a 4-bladed propeller, which is used as the base case for this project.

4.1 GPU Parallelization

The binning approach was successfully implemented with a single time loop. This allowed the parallelization of the time dimension, which wasn't possible in the previous version. The time dimension was chosen as the outer most loop of the algorithm and therefore, it was asigned for the x-direction of the GPU thread structure. Observers and source elements were assigned to the y and z directions, respectively. Initially, there was an error with the time parallelization and lead to erroneous acoustic pressure values. The reason for this was found out to be the accessing of the same memory location by multiple GPU threads at the same time due to the binning approach. This is a common issue with GPU parallelization and is called a race condition. The solution is to use atomic functions, which are a set of functions that are supported by CUDA to be carried out at the thread level without interruption by other threads [15]. It is a hardware based solution and is supported by CUDA 6.0 and above. In this case, since it requires multiple threads to update the same memory location by solutions computed at them, atomic addition needs to be used. However, only Tesla P100, Pascal, Tesla V100 and Titan V GPUs support double precision in atomic functions. Therefore, for the code to be used without any hardware restrictions, single precision was used. This not only solved the issue, but also saved memory usage and computation time. For validation of the binning approach and to ensure the code is free from bugs, a comparison was done with the results from ACUM-2 for the base case and the OASPL distributions are given in

Figure 4.1. The curves for both loading and thickness noises from the two versions match with other perfectly, proving the GPU parallelization was successful.
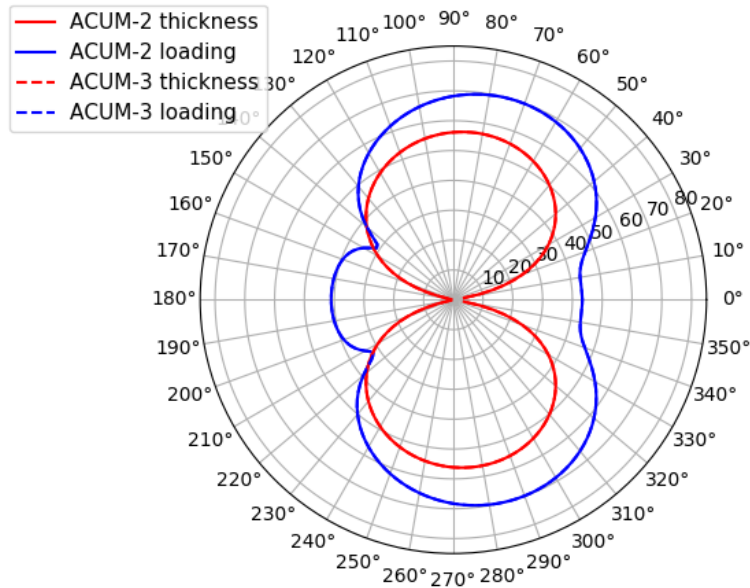

Figure 4.1: Validation of ACUM-3 using the base case

4.2 Computation Time Optimization

As the final goal of ACUM-3 is to run acoustic simulations for long durations it is very important that it spends the least amount of time on computation to have a reasonable computation time for longer simulations. Obviously, 3D GPU parallelization lead to the largest reduction in computation time. Switching from double precision to single precision also lead to a reduction in the computation time by about 15%. Here, the majority of the reduction came from reading the input files and the GPU calculation.

Next, another considerable improvement was made by using the coarser mesh for the acoustic computation instead of the one used in CFD. The original surface mesh developed for the CFD simulation has both triangular and quadrilateral surface elements. This is then subdivided to form a fully quadrilateral mesh in the volume mesh generation stage and that is what is used in the CFD simulation. For the purpose of saving ACUM-3 inputs on the coarser mesh, its connectivity data was set to be read by HAMSTR at the onset of the CFD simulation. Using these data, the CFD solver can write the outputs pertaining to the elements of this mesh in the output files. This saved the computation time by about 77% for the base case.

The Farassat's 1A formulation of the Ffowcs Williams-Hawkings eqaution has two forms: permeable and impermeable. The permeable formulation considers an imaginary surface (permeable) enclosing the actual physical surface as the acoustic surface. The impermeable formulation take the actual physical surface as the acoustic surface. ACUM-2 had provisions to use either of them

in the acoustic simulation. In the permeable formulation, the solver needs the flow velocity (three variables for the three directions) and local density at the imaginary surface. Therefore, including the local pressure, the acoustic solver needs to read five variables from the CFD simulation if it uses the permeable formulation. These variables have to be filtered using a Gaussian and median filter to filter out the high frequency noise in order to do accurate derivative computations. In the impermeable formulation the flow velocity is always equal to the surface velocity and therefore, all terms in the formulation containing the flow velocity and local density cancel out. Therefore, by removing of the option for the permeable formulation, ACUM-3 was able to do the computation using only the surface pressure and get rid of the reading and processing of the other four CFD variables. This lead to a 37% reduction in computation time with the majority coming from the pre-processing stage. A summary of the computation time optimization with the percentage reduction in each stage is given in Table 4.1. At the end of all these modifications, the computation time was reduced by 98% from that of ACUM-2.

Table 4.1: Summary of computation time optimization

Upgrade	Computation Time (s)	Reduction	Total Reduction
ACUM-2	2462.9	-	-
ACUM-2 w/ 2D parallelization	531.1	78.4%	78.4%
ACUM-2 w/ coarsening	122.6	76.9%	95.0%
ACUM-3 w/ 3D parallelization	90.0	26.6%	96.3%
ACUM-3 w/ impermeable approach	57.0	89.4%	97.7%
ACUM-3 w/ single precision	48.5	60.4%	98.0%

4.3 MPI Parallelizaion

A single GPU is not able to handle long duration simulations due to limitations in speed and memory. Therefore, ACUM-3 was designed to distribute it's workload onto multiple nodes on a HPC cluster with multiple GPU's using MPI. Bluecrab, which is the HPC cluster located at the Johns Hopkins University and shared with the University of Maryland, was selected for this purpose, as the in-house CFD solver is also located in this HPC cluster it would avoid the need to copy the CFD output files from one place to another.

Bluecrab has two Tesla K80 GPUs per node with each having a memory of 24 GB. In the base case, each blade with 12,000 elements uses about 1.2 GB per revolution with 360 time steps. Therefore, each CFD output file can contain up to 15 to 20 revolutions. Using five nodes at a time, 150 to 200 revolutions can be parallelized. Therefore, this provides sufficient computational power to run ACUM-3 for a reasonable amount of duration to simulate non-periodic cases. The computation time of ACUM-3 in bluecrab was compared with that in a single node. It was found that Bluecrab takes 60% more time to read files as the files are saved on a different node from the one that is doing the computation. It spends 24% less time on the GPU computation due to its superior GPUs. Therefore, to negate the effect of reading inputs it was decided to share the workload among multiple CPU cores.

The CFD solver was set to write one output file per each surface and each chunk of time steps so that it can be directly read by ACUM-3 without a post-processor. The number of time steps per

chunk can be determined by the number of elements of the surface and the memory limitation of the GPU. Each CPU core or processing element (PE) reads and pre-processes one CFD output file at a time. If the number of PEs used is less than the product of the number of time step chunks and the number of surfaces, the computation will be done on a rolling basis until every chunk and surface is processed. The number of PEs used in a node can be more than the number of GPUs in that node, allowing the GPUs to be shared between the multiple CPUs. Since the time spent to read input files is greater than the time spent on the GPU computation, this allows some PEs to read and pre-process inputs while others use the GPU. This ensures the optimum utilization of computational resources. During the computation each PE was set to record its solutions in two large arrays assigned to thickness and loading acoustic pressure, which accommodate all the time steps and observer locations. At the end of the computation, each PE sends the two arrays to PE_0 through the MPI command MPI_Reduce(). Finally, PE_0 writes the solution arrays into output files. Unlike in ACUM-2, it also computes the OASPL inside the solver using the nearest time steps that covers a revolution and writes the solutions into separate output files.

4.4 Additional Data Requirements

As the binning computation at each time step requires information about the two neighboring time steps, each time step chunk needs to have input data for one time step before its first time step and one after its last time step except for the time steps at the beginning and the end of the solution time history. These data was included in the output files at the CFD stage so that PE's do not have to communicate with each other during the acoustic computation.

In periodic acoustic computations the complete solutions can be obtained for the full time history for which input data is available. But this is not the case for non-periodic computations. A source surface has multiple elements and therefore, the pressure signals they emit take different times to reach an observer. If we consider the first time step, the solution time history would be incomplete until the pressure signal from the farthest source element arrives at the observer as there is no input data for a time step prior to that. Therefore, the solution time history after this point of time can only be considered as complete. Similarly, there would be point of time pertaining to the last time step and the source element closest to the observer, after which the solution would be incomplete. Therefore, the solution time history needs to be truncated at the two ends for it to be complete.

4.5 Validation

ACUM-3 was validated using the base case of the 4-bladed propeller by comparing its thickness acoustic pressure time history with that of ACUM-2. Four observer locations were selected for elevation angles $30°$, $45°$, $60°$, and $80°$ along the circular set of observers in Figure 2.2(b). Figure 4.2 presents the thickness acoustic pressure time history at these observers computed from ACUM-2 and ACUM-3. Figure 4.2(b) shows the same variation in the thickness acoustic pressure as Figure 4.2(a), proving the accuracy of ACUM-3. Figure 4.2(b) shows only part of the solution in Figure 4.2(a) because of the truncation at the two edges. Figure 4.2(c) presents the thickness acoustic pressure variation for three revolutions. Since it is using the same input data it is simply an extension of the same variation.

4.6 Flyover Simulation

The first non-periodic case considered is the flyover, where the propeller is set to fly for 100 revolutions passing a set of observers located at 2, 5, 10, 30, 60, 100, 200, and 500 times the propeller radius (R) from the path of the propeller center. The observers are located in a straight line perpendicular to the path of the propeller center. Since the propeller flies in a steady configuration, the aerodynamic data would be the same for each revolution, and therefore, CFD data is needed for only one revolution. Therefore, ACUM-3 was modified to treat the flyover case separately. It reads inputs at the beginning and uses the same data for all revolutions, updating the source locations as the propeller moves forward at each time step. The pressure time history was computed for all 100 revolutions. Four CPU cores and four GPUs were used in the computation, which took only 3 minutes because of not having to read input data for each revolution. The instantaneous OASPL was calculated at each time step from the acoustic pressure time history using the nearest time steps that cover a full revolution. The acoustic pressure time history, which is given in Figure 4.3, shows that the loading acoustic pressure is the dominant component of the total noise. Both loading and thickness pressure fluctuation amplitude increases as the propeller flies closer to the observers, where they actually lie on the plane of the propeller. Figure 3.1 confirms this by having the largest noise on the plane of the propeller.

The loading and thickness components of the instantaneous OASPL are given in Figure 4.4. The thickness component is much lower than the loading component at all times for all observer locations as it should be. Observers closer than 30R to the propeller path shows a sharp rise in both noise components as the propeller passes the line of observers. This is because for the observers closer to the propeller path the elevation angle is in between 180° and 215° at the beginning, where the noise is low (refer to Figure 3.1) and it increases to about 330°-360° passing a region, where the noise is higher. The closer the observer is to the propeller path, the quicker it goes through the elevation angles, increasing the sharpness of the increase and the maximum noise. As the observer distance increases up to around 60R, the average noise level increases, as the observer stays within the range of elevation angles where the noise level is high. However, as the observer distance increases further, distance comes into play, resulting in a lower noise level.

5 Modifications to CFD solver

The second part of the project was to modify the in-house CFD solver to efficiently write output files that are needed as inputs for ACUM-3 and to include non-linear, non-periodic motion capability.

5.1 Modification for Optimum Output

Previously, surface outputs were written at each time step of the CFD simulations and a post-processing script was used to pick only the data needed for the acoustic computation and combine data for one revolution for each surface. Writing output at each time step consumes a lot of time in the CFD simulation and makes it difficult to run simulations for more than a couple of revolutions in one go. Therefore, running 30-50 revolutions this way is not possible. On the other hand, it would result in a huge number of output files that needed to be post-processed, which consumes both time and memory, unnecessarily. Therefore, the post-processing part was integrated to the CFD solver to write output files for each surface and time step chunk that can be directly readable
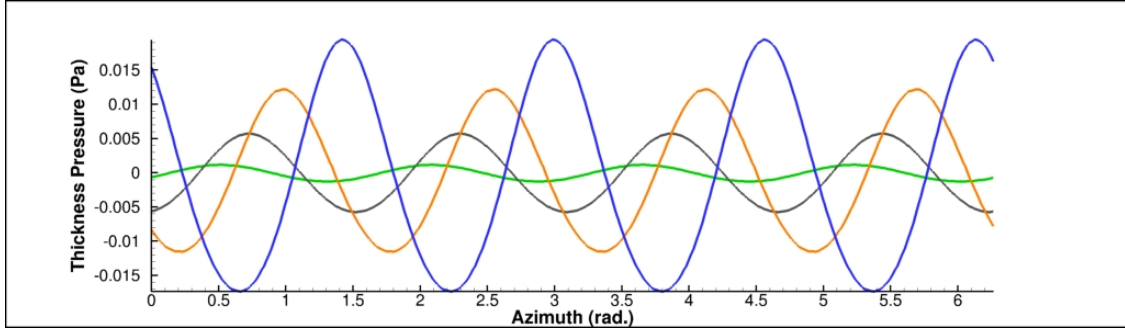
(a) One revolution from ACUM-2
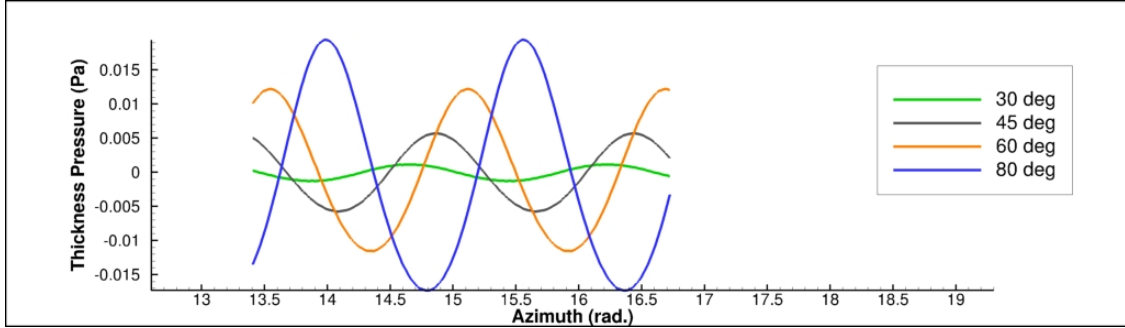

(b) One revolution from ACUM-3
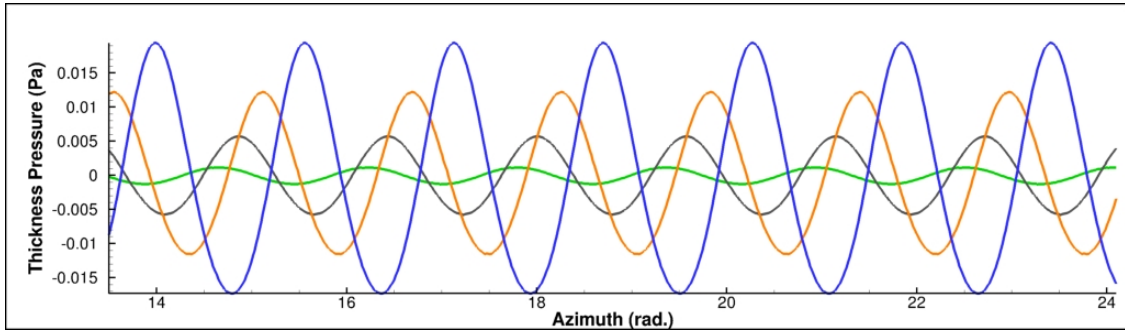
(c) Three revolutions from ACUM-3

Figure 4.2: Comparison of thickness acoustic pressure time history

by ACUM-3. This saves a lot of computation time.

5.2 Non-Periodic Motion

The major modification to CFD came in the form of adding non-linear, non-periodic motion caoability, required to simulate non-periodic cases. The in-house CFD package consists of four basic solvers. The main platform is known as the Mercury framework [16], which facilitates an overset mesh system that can be solved by different solvers. It serves as the "core" of the CFD package. Based on the type of mesh that needs to be solved, different solvers can be used inside the Mercury core. The Graphics Processing Unit Accelerated Rotor Flow Field Solver (GARFIELD) [17] is used for structured meshes, whereas Hamiltonian/Strand solver (HAMSTR) [12] is used for unstructured nearbody meshes. The connectivity between the different overset meshes is performed using the
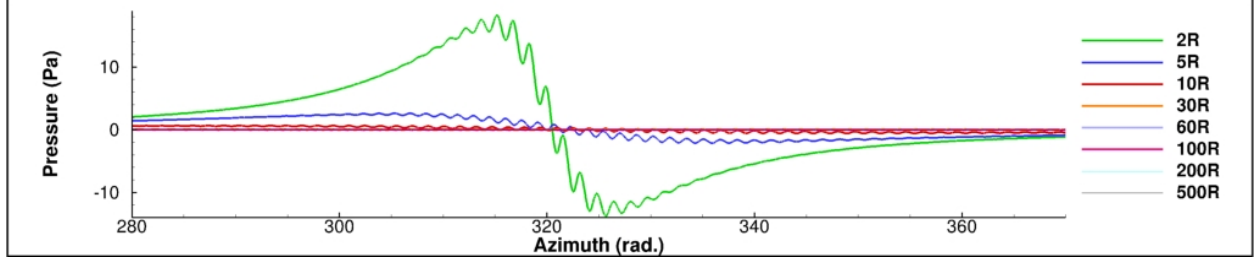
(a) Total acoustic pressure time history
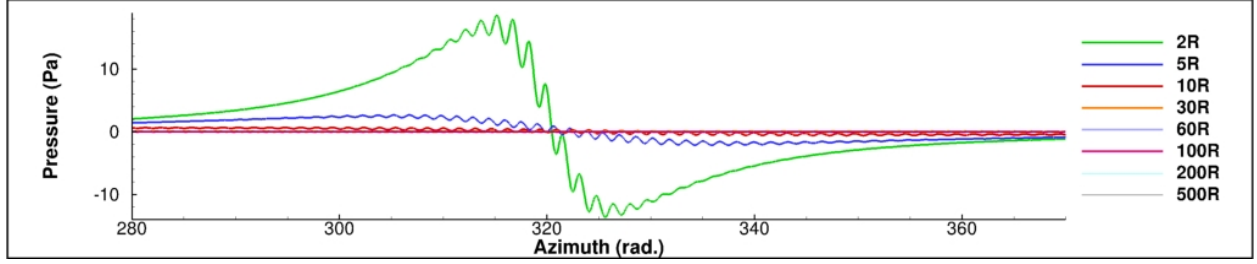
(b) Loading acoustic pressure time history
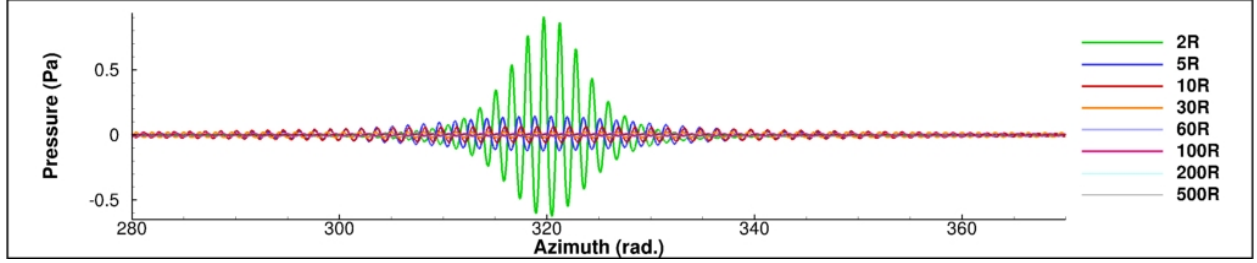
(c) Thickness acoustic pressure time history

Figure 4.3: Acoustic pressure time history for the flyover case

Topology Independent Overset Grid Assembler (TIOGA) [18], which creates iblank arrays at the boundaries and passes interpolated flow quantities between the meshes.

Mesh motion is handled by the Mercury core using a separate module known as the "Motion" module. It is a python/C++ wrapper and only performs periodic mesh movements such as rotation about an axis and elastic deflections. It uses matrix multiplications to perform 3D rotations but has provisions only for rotation around z-axis. Therefore, it uses a frame matrix to map any other rotational axis to z-axis. The equation used for matrix rotation is given in Eq. 13.

$$X_{i+1} = FR_{i+1}(FR_i)^{-1}X_i \qquad (13)$$

where,

$$X_i = \begin{bmatrix} x \\ y \\ z \\ 1 \end{bmatrix} \qquad (14)$$

is the coordinate vector of each mesh element. Here, i represents the current time step and $i+1$ represents the next time step. F and R are the frame and rotational matrices, respectively. Rotational matrix is given in Eq. 16.
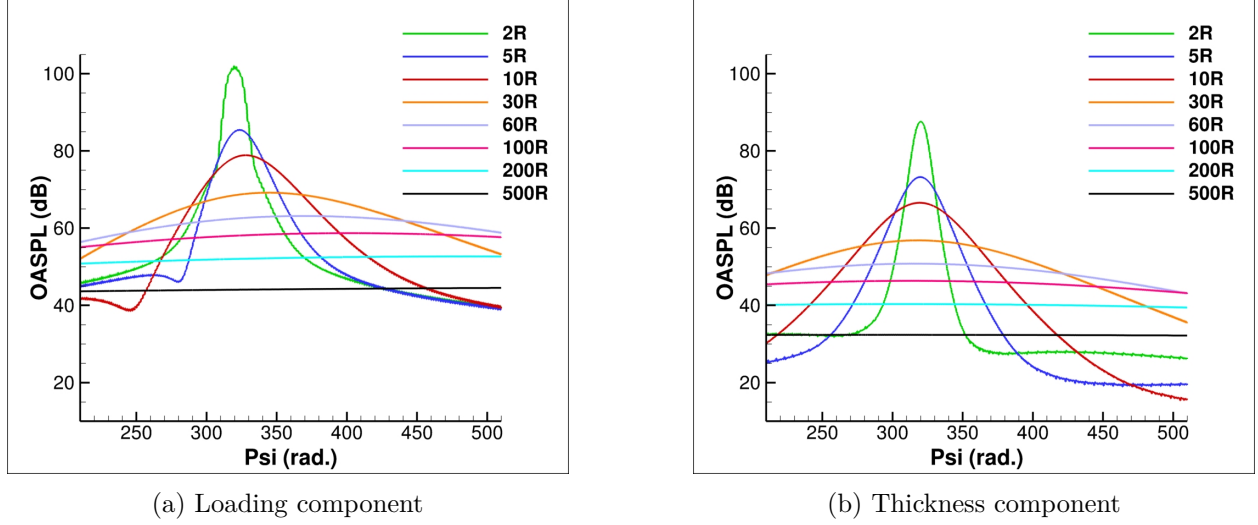
(a) Loading component
(b) Thickness component

Figure 4.4: Instantaneous OASPL for the flyover case

$$R = \begin{bmatrix} cos\theta & -sin\theta & 0 & 0 \\ sin\theta & cos\theta & 0 & 0 \\ 0 & 0 & 1 & 0 \\ 0 & 0 & 0 & 1 \end{bmatrix} \tag{15}$$

Motion module has no provisions for accelerations multi-axial rotation and translation. A non-periodic motion such as transition from hover to cruise includes two rotating motions, one about the propeller axis and the other about the wing pitch axis as shown in Figure 5.1. It also involves accelerated translation as it starts to move forward. The RPM of the proprotor can also be changed to balance the lift and drag. This is because in hover, the propeller thrust balances the weight of the tiltrotor, whereas in cruise, it balances the drag of the fuselage. Therefore, a new motion module was created to incorporate non-periodic motions to the CFD simulations. The motion of a mesh element is performed in two stages, which are given in Eq. 16 and 17.

$$X'_{i+1} = T_{i+1}F^{[1]}R^{[1]}_{i+1}(T_iF^{[1]}R^{[1]}_i)^{-1}X_i \tag{16}$$

$$X_{i+1} = T_{i+1}F^{[2]}R^{[2]}_{i+1}(T_{i+1}F^{[2]}R^{[2]}_i)^{-1}X'_{i+1} \tag{17}$$

where,

$$F^{[2]} = F^{[1]}R^{[1]}_{i+1}(F^{[1]})^{-1}F^{[2,0]} \tag{18}$$

Here, $F^{[2,0]}$ is the original frame matrix for the secondary rotation. The superscripts [1] and [2] refer to matrices of the primary and secondary rotation, respectively. T is the translation matrix. Figure 5.2 shows the accelerated multi-axial rotation of a single blade, achieved using this updated module. Figure 5.3 shows the translation of the blade on top of the multi-axial rotation.

6 Simulation of Non-Periodic Cases

At the beginning of the project it was expected to run several non-periodic cases such as take-off and landing, propeller RPM change, propeller angle change etc. However, due to the time
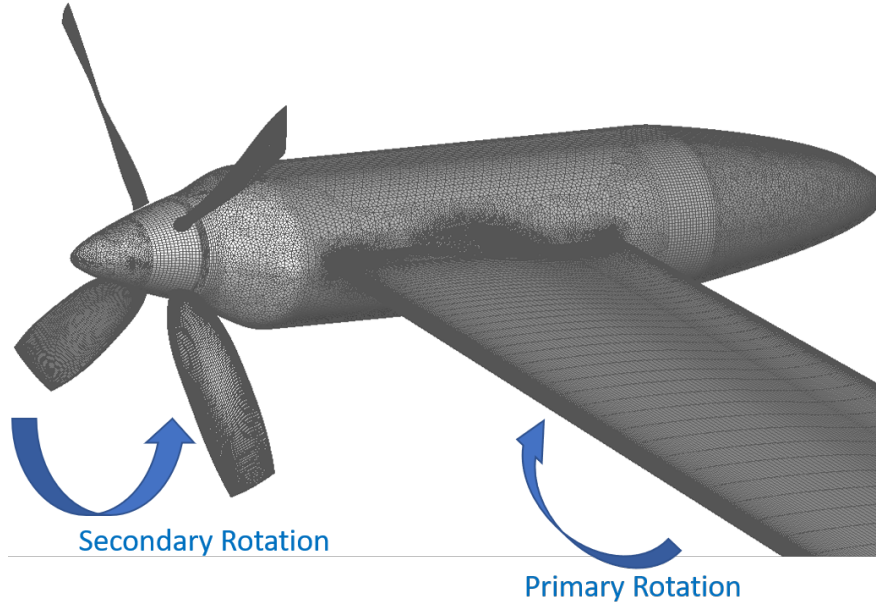
Figure 5.1: Primary and secondary rotations in proprotor transition

limitation, the non-periodic simulation part had to be restricted to one case. The transition of a proprotor from hover to cruise, which is shown in Figure 6.1 was identified to simulate most of the non-periodic events, and therefore was studied under this project.

6.1 Case Description

Quasi-steady simulations were performed at $0°$ (hover), $45°$ and $90°$ (cruise) to have periodic results to compare with the unsteady simulation. Separate CFD simulations were run at each propeller angle for the 4-bladed propeller and the results were used as inputs for ACUM3-periodic to obtain the respective periodic acoustic solutions.

Transition from hover to cruise take usually about 5 seconds and at the current RPM of 98.42 Hz, this adds up to nearly 500 propeller revolutions and would take up to 90 days to run. Therefore, it was decided to reduce the RPM to 30 Hz to reduce the computational time. However, this ended up producing a negative thrust in cruise due to lower RPM and had insufficient noise levels for the purpose of investigation. Therefore, it was decided to go with the original RPM of 98.42 Hz and decrease the transition time to 1 second. Even though this was not very realistic, it was decided to go with this due to the time and resource limitations. The rotational speed of the propeller was set to reduce from 1.3 x 98.42 Hz to 98.42 Hz over the course of 100 revolutions. The forward speed was set to increase from 0 Mach to 0.08 Mach. A constant time step size was used, which is equal to the time step size in the $45°$ case with a $2°$ time step.
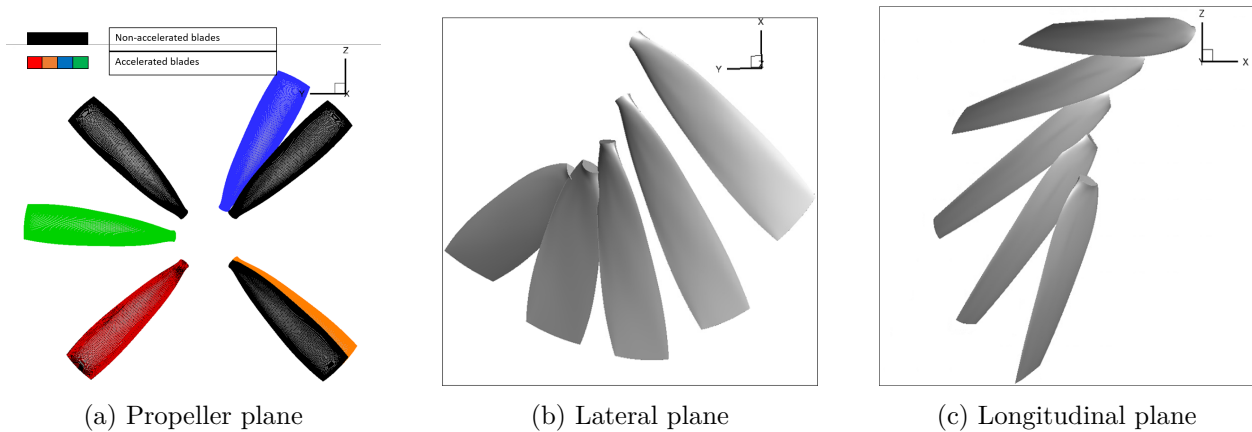
| (a) Propeller plane | (b) Lateral plane | (c) Longitudinal plane |

Figure 5.2: Accelerated multi-axial rotation
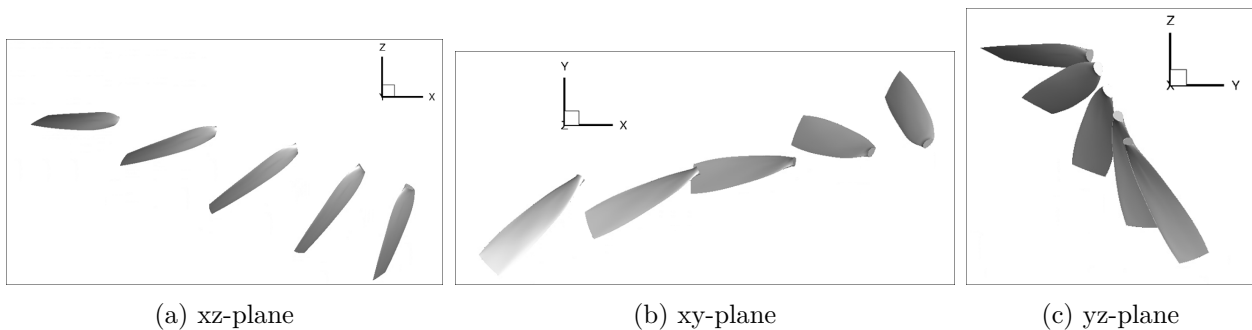

| (a) xz-plane | (b) xy-plane | (c) yz-plane |

Figure 5.3: Translation and multi-axial rotation

6.2 Results

6.2.1 Quasi-Steady Cases

The flow pathlines and the vorticity contours for the three quasi-steady cases are presented in Figure 6.2. The propeller wake flows away from the propeller as the freestream velocity increases from hover to cruise. In hover, the blade wake interacts with other blades causing unsteady surface pressure distributions that could potentially cause high loading noise. In cruise there is no wake interaction and therefore, the loading noise is expected to be less. The RPM decrease as the propeller transitions from hover to cruise is also expected to decrease both loading and thickness noise levels.

Figure 6.3 presents the coefficient of thrust for the propeller and individual blades for the three quasi-steady cases. Hover provides the highest thrust in order to balance the lift provided by the wing in cruise. The factor of 1.3 was used to account for this difference in thrust produced.

Figure 6.4 depicts the loading, thickness and total noise levels for hover and 45° cases and the total noise level comparison with cruise. It shows the reduction in noise levels as the propeller transitions from hover to cruise, which was expected. Even though both hover and cruise OASPL curves show symmetry around the propeller axis, the 45° case shows asymmetry due to the inclination to freestream.
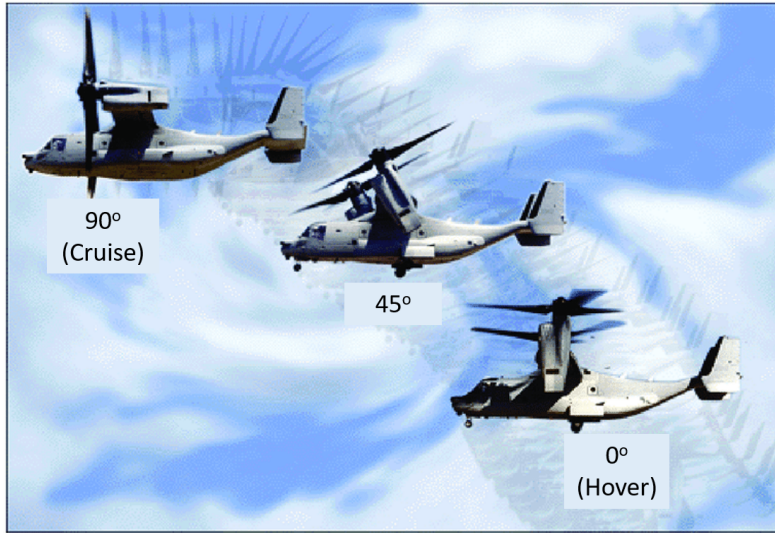
Figure 6.1: Primary and secondary rotations in proprotor transition

6.2.2 Unsteady Case

Due to the time limitations, the results for the complete unsteady simulation of 100 propeller revolutions are not available at the time this report is written. Therefore, the initial portion of the results for the first few propeller revolutions is presented here. Figure 6.5(a) presents the vorticity contours for the unsteady case, showing blade-wake interaction. Figure 6.5(b) shows the thickness acoustic pressure time history at the in-plane observer for the unsteady case compared with that for the three quasi steady cases. As the transition case is still in its early revolutions its magnitude is closer to the hover curve. The phase difference is due to the misalignment of the starting points of the time history since the unsteady case truncates part of the time history.

Figure 6.5(c) shows the variation in sound pressure level (SPL) with time for the transition case and is compared with the constant value obtained for hover. The SPL for the unsteady case is obtained by considering acoustic pressure fluctuation over the nearest 180 time steps. The result fall within 0.4% deviation from the hover case at the beginning, and continues to drop as the RPM reduces, which is expected.

7 Conclusion

The project was focused on creating a CFD - computational aerocoustics platform to simulate non-periodic aircraft maneuvers and calculate the noise signatures. The in-house acoustic code, ACUM, was upgraded to perform acoustic calculations for a large number of time steps by parallelizing the time, observer and source element dimensions across GPUs and CPUs. A new version of the ACUM was created to reduce the computation time and perform the acoustic computation at an enhanced efficiency. It is now capable of performing periodic, non-periodic and semi-periodic simulations such as flyovers at a higher computational speed.
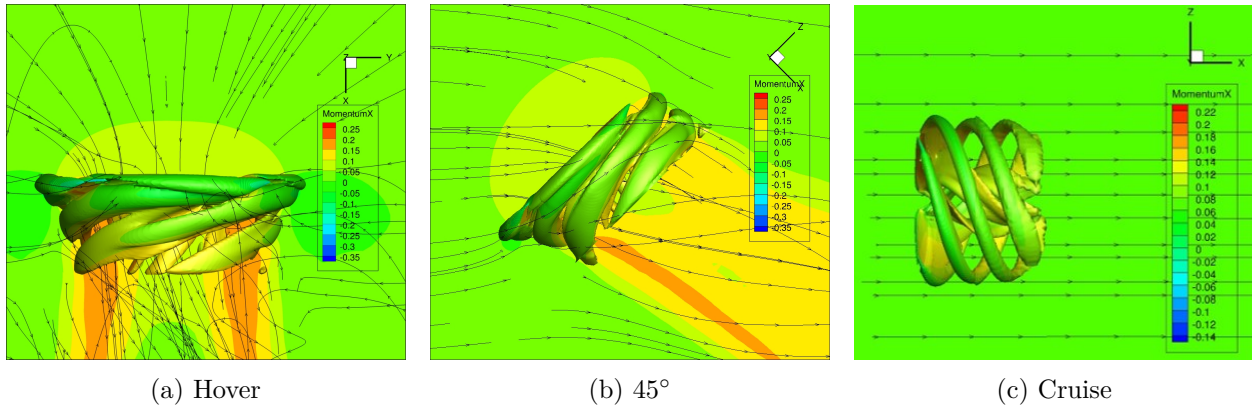
(a) Hover   (b) 45°   (c) Cruise

Figure 6.2: Vorticity contours and pathlines for the three quasi-steady cases
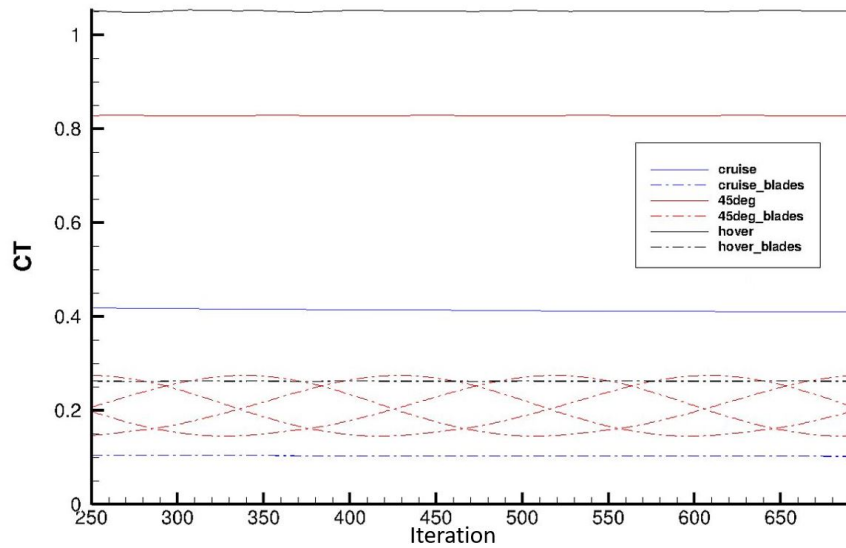

Figure 6.3: Coefficient of Thrust for propeller and individual blades in the three quasi-steady cases

The in-house CFD code was also updated to include the non-periodic, non-linear motion capability by creating a new "Motion" module. This enabled translation, accelerated rotation, and multi-axial rotation that was necessary to simulate most non-periodic movements.

Finally, the new framework was used to simulate a proprotor transitioning from hover to cruise. The simulation was not able to be completed due to time and resource limitations. However, the initial results look promising.

8 Future Work

As the unsteady transition simulation will be completed over the coming weeks and the results will be compared against the quasi-steady results for 45° and cruise cases. After that the whole geometry which consists of the propeller and the wing will be simulated to understand the effects

(a) Hover

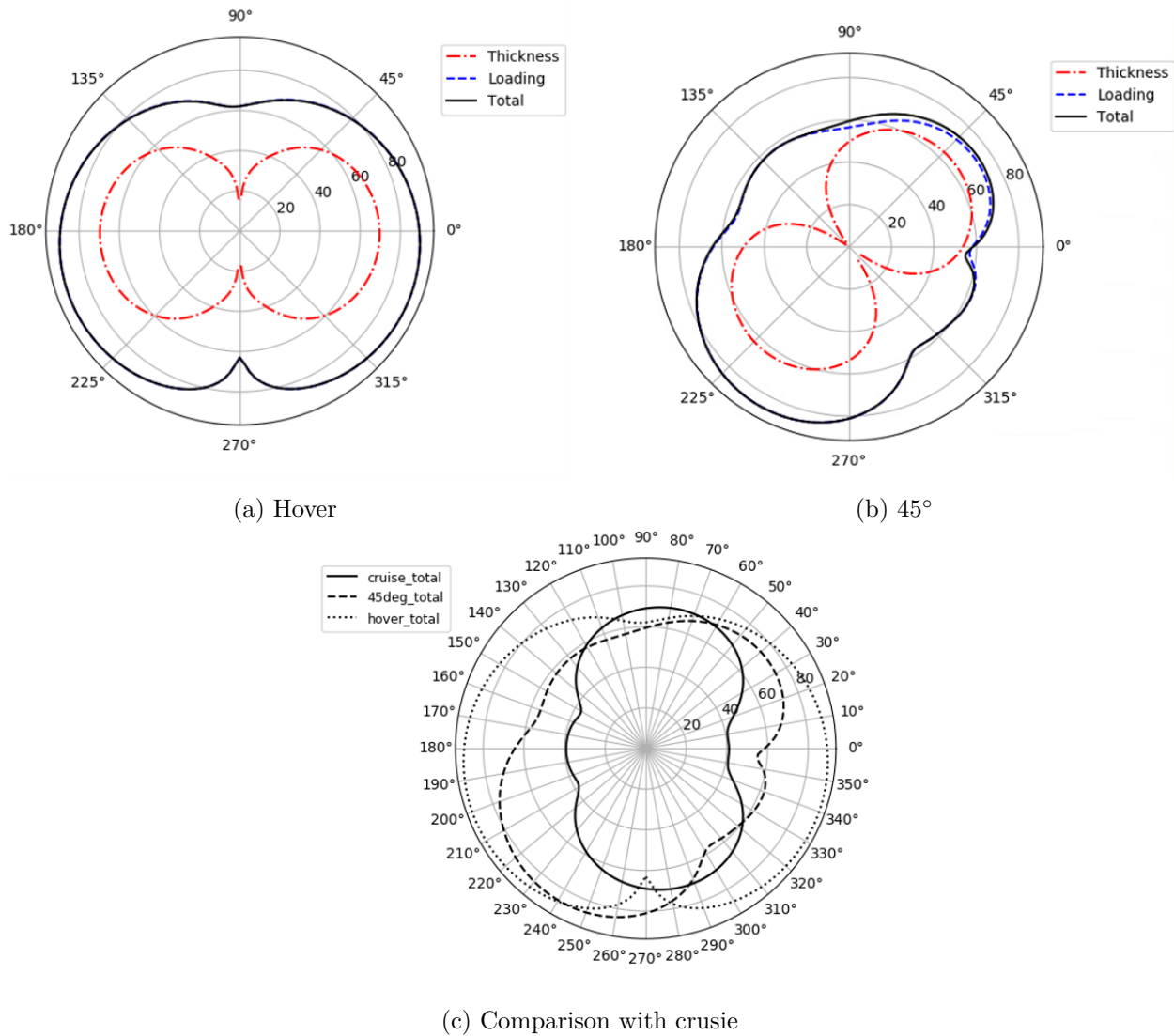(b) 45°

(c) Comparison with crusie

Figure 6.4: OASPL in dB for quasi-steady cases

of transition on the wing and vice versa.

It was understood that the use of CFD for the purpose of simulating acoustics is too expensive and time consuming. Therefore, other methods of determining surface pressure such as vortex methods will be evaluated and will be used to replace or assist the CFD part of this framework.

To achieve a comprehensive understanding of how aircraft noise is felt in an urban environment, it is necessary to simulate some of its main features such as tall buildings. Reflection of the acoustic pressure waves off building surfaces could potentially make a significant affect on the noise observed by a pedestrian. Therefore, it is important for ACUM-3 to have the capability to account for the reflecting noise as well. This can be done by modelling building surfaces as reflectors for upcoming acoustic waves.
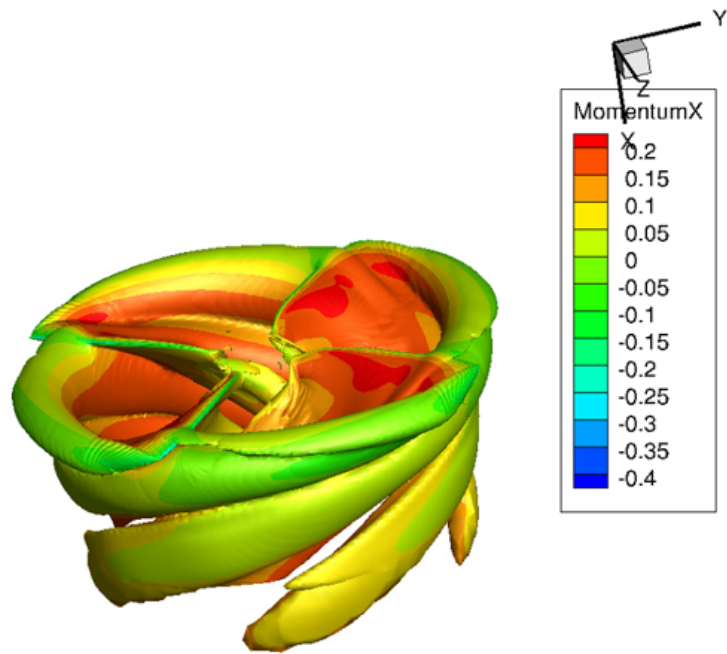
(a) Vorticity contour for unsteady propeller case
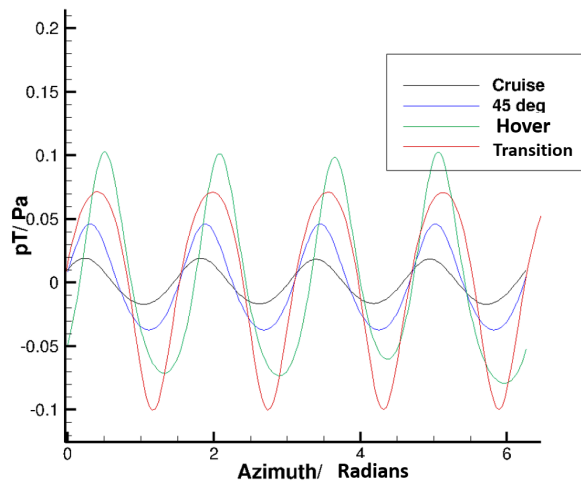
(b) Thickness acoustic pressure time history for all cases at the in-plane observer
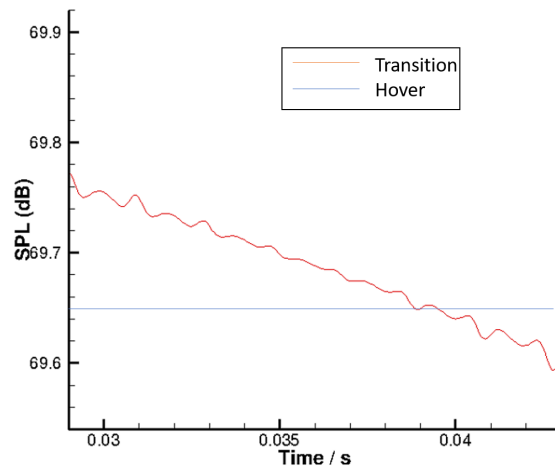
(c) Thickness sound pressure level for unsteady transition case and hover case

Figure 6.5: Results for the unsteady transition case

References

[1] https://www.nasa.gov/aero/taking-air-travel-to-the-streets-or-just-above-them/.

[2] https://www.nasa.gov/specials/X57/.

[3] https://www.uber.com/us/en/elevate/.

[4] Guynn, M. D., Berton, J. J., Haller, W. J., Hendricks, E. S., and Tong, M. T., "Performance and Environmental Assessment of an Advanced Aircraft with Open Rotor Propulsion," NASA TM 217772, 2012.

[5] Sinnige, T., de Vries, R., Corte, B. D., Avallone, F., Ragni, D., Eitelberg, G., and Veldhuis, L. L., "Unsteady Pylon Loading Caused by Propeller-Slipstream Impingement for Tip-Mounted Propellers," *Journal of Aircraft*, Vol. 55, (4), 2018, pp. 1605–1618.

[6] Zolbayar, B. E., *Investigation of Noise from Electric, Low-Tip-Speed Aircraft Propellers*, Master's thesis, Penn State University, State College, 2018.

[7] Ffowcs Williams, J. E., and Hawkings, D. L., "Sound Generation by Turbulence and Surfaces in Arbitrary Motion," *Philosophical Transactions of the Royal Society of London. Series A, Mathematical and Physical Sciences*, Vol. 264, (1151), 1969, pp. 321–342.

[8] Hanson, D. B., and Fink, M. R., "The importance of quadrupole sources in prediction of transonic tip speed propeller noise," *Journal of Sound and Vibration*, Vol. 62, (1), 1979, pp. 19–38.

[9] Farassat, F., "Derivation of Formulations 1 and 1A of Farassat," , 2007.

[10] Phillips, W. F., *Mechanics of Flight*, second edition, 2009.

[11] Baeder, J., "Passive design for isolated blade-vortex interaction noise reduction," ANNUAL FORUM PROCEEDINGS-AMERICAN HELICOPTER SOCIETY, Vol. 53, 1997.

[12] Jung, Y. S., Govindarajan, B., and Baeder, J., "Turbulent and Unsteady Flows on Unstructured Line-Based Hamiltonian Paths and Strands Grids," *AIAA Journal*, Vol. 55, (6), 2017, pp. 1986–2001.

[13] Amiraux, M., *Numerical Simulation and Validation of Helicopter Blade-Vortex Interaction Using Coupled CFD/CSD and Three Levels of Aerodynamic Modeling*, Ph.D. thesis, University of Maryland, College Park, 2014.

[14] "Wind Tunnel Testing of Propeller Wingtip Interactions," Helden Aerospace, LLC and Empirical Systems Aerospace, Inc., 2019.

[15] Cooper, C., "GPU Computing with CUDA Lecture 3 - Efficient Shared Memory Use," University Lecture, 2011.

[16] Jude, D., Lee, B., Jung, Y. S., Petermann, J., Govindarajan, B., and Baeder, J., "Application of a Heterogeneous CFD Framework Towards Simulating Complete Rotorcraft Configurations," American Helicopter Society, 74th Annual Forum Proceedings, Phoenix, Arizona, May 14-17, 2018.

[17] Jude, D., and Baeder, J. D., "Extending a Three-Dimensional GPU RANS Solver for Unsteady Grid Motion and Free-Wake Coupling," 54th AIAA Aerospace Sciences Meeting, 2016.

[18] Brazell, M. J., Sitaraman, J., and Mavriplis, D. J., "An Overset Mesh Approach for 3D Mixed Element High-Order Discretizations," *Journal of Computational Physics*, Vol. 322, 2016, pp. 33–51.